



The Spatial Correlation between CN-line- and Dust-continuum-emitting Regions in High-mass Star-forming Clouds

Jihye Hwang¹, Chang Won Lee^{1,2}, Jongsoo Kim¹, Eun Jung Chung³, and Kee-Tae Kim^{1,2}¹ Korea Astronomy and Space Science Institute (KASI), 776 Daedeokdae-ro, Yuseong-gu, Daejeon 34055, Republic of Korea; hjh3772@gmail.com² University of Science and Technology, Korea (UST), 217 Gajeong-ro, Yuseong-gu, Daejeon 34113, Republic of Korea³ Department of Astronomy and Space Science, Chungnam National University, 99 Daehak-ro, Yuseong-gu, Daejeon 34134, Republic of Korea

Received 2023 December 31; revised 2024 August 14; accepted 2024 August 14; published 2024 October 15

Abstract

Measuring the strength of a three-dimensional (3D) magnetic field vector is challenging as it is not easy to recognize whether its line-of-sight (LOS) and plane-of-sky (POS) components are obtained from the same region. CN ($N=1-0$) emission has been used to get the LOS component of a magnetic field (B_{LOS}) from its Zeeman splitting lines, while dust continuum emission has been used to get the POS component of a magnetic field (B_{POS}). We use the CN ($N=1-0$) data observed with the Taeduk Radio Astronomy Observatory 14 m telescope and the dust continuum data from the Herschel archive toward six high-mass star-forming regions in order to test whether CN line and dust continuum emission can trace a similar region and thus can be used for inferring 3D magnetic field strength. Our comparison between CN and H_2 column densities for all targets indicates that CN line emission tends to be strong toward bright continuum regions. The positions of peak CN column densities are particularly well correlated with those of peak H_2 column densities, at least over the H_2 column density of $8.0 \times 10^{22} \text{ cm}^{-2}$ within one or two telescope beam sizes in all targets, implying that CN-line- and dust-continuum-emitting regions are likely spatially coincident. This enabled us to make the reliable measurement of the 3D magnetic field strengths of five targets by taking a vector sum of their B_{LOS} and B_{POS} , helping to decide the magnetical criticality of the targets as supercritical or transcritical.

Unified Astronomy Thesaurus concepts: [Molecular clouds \(1072\)](#); [Magnetic fields \(994\)](#); [Interstellar medium \(847\)](#); [Star formation \(1569\)](#)

1. Introduction

Magnetic fields play important roles in star-forming processes by supporting star-forming regions against gravitational collapse and regulating core fragmentation (e.g., T. C. Mouschovias et al. 2006; J. Hwang et al. 2021, 2022, references in K. Pattle et al. 2023). To judge the importance of a magnetic field compared with turbulence and gravity, it is necessary to measure their three-dimensional (3D) magnetic field strengths (e.g., T. C. Mouschovias & L. Spitzer 1976; R. M. Crutcher et al. 2004). However, it is a challenging task to directly estimate the 3D magnetic field strengths of star-forming regions.

The plane-of-the-sky (POS) and the line-of-sight (LOS) components of the magnetic fields in star-forming regions can be measured by observations of dust polarized emission (e.g., K. Pattle et al. 2023, and references therein) and Zeeman effect in line emission (e.g., R. M. Crutcher & A. J. Kemball 2019, and references therein), respectively. The measurement of the POS component of a magnetic field is based on the assumption that the minor axis of a dust grain is aligned along a magnetic field line by the radiative alignment torques (A. Lazarian & T. Hoang 2007) and the dust continuum is preferentially emitted (polarized) perpendicular to the magnetic field in the POS (B.-G. Andersson et al. 2015). The magnetic field strength in the POS component has been estimated by the Davis–Chandrasekhar–Fermi (DCF; L. Davis 1951; S. Chandrasekhar & E. Fermi 1953) method. In the method, magnetic field lines

are assumed to be initially uniform and distorted by nonthermal gas motion, and thus the magnetic field strength can be estimated on a hypothesis that polarization angle dispersion would indicate the distortion of the magnetic field lines by the nonthermal gas motion (e.g., K. Pattle & L. Fissel 2019; K. Pattle et al. 2023). The LOS component of the magnetic field can be measured by the Zeeman effect of a molecular line tracer whose energy levels are split under the magnetic field. Spectral lines of HI, OH, CN, and masers lines of CH_3OH and H_2O are known to be the tracers showing the Zeeman effects and thus have been used to estimate the LOS magnetic field strengths in star-forming regions (e.g., R. M. Crutcher & A. J. Kemball 2019). In principle, by taking the vector sum of the POS and LOS components, 3D magnetic field strengths in star-forming regions can be obtained, but their practical measurement has been rare and difficult.

There are a few attempts to estimate 3D magnetic field orientations and strengths. P. C. Myers & A. A. Goodman (1991) and A. A. Goodman & C. Heiles (1994) measured the 3D magnetic field strengths in dark cloud complexes by using observations of optical dust polarization and Zeeman effect of HI and OH, which trace diffuse regions ($n_{\text{H}} \sim 10\text{--}10^3 \text{ cm}^{-3}$). The 3D magnetic field in a star-forming region, Barnard 1, was estimated using OH Zeeman effect and dust polarized emission obtained by SCUPOL and POL-2 (A. A. Goodman et al. 1989; S. Coudé et al. 2019; B. C. Matthews & C. D. Wilson 2002). There is one attempt to measure the 3D magnetic field strength in a dense star-forming clump G35.20w in W48 (T. Pillai et al. 2016) with the vector sum of both POS and LOS magnetic field strengths measured by dust polarized emission and CN Zeeman effect. Another attempt to measure the 3D magnetic field toward NGC 1333 has been made by combining the results



Original content from this work may be used under the terms of the [Creative Commons Attribution 4.0 licence](#). Any further distribution of this work must maintain attribution to the author(s) and the title of the work, journal citation and DOI.

from dust polarization data and toy models, assuming a morphology of magnetic field lines perpendicular to filament structures in NGC 1333 (Y. Doi et al. 2020, 2021).

One of the important assumptions made in estimating the 3D magnetic field strength using the vector sum is that POS and LOS components of a magnetic field would come from a physically similar region. Therefore, it is necessary to check whether dust emission and Zeeman splitting line emission trace the common region. In this paper, we attempt to investigate how dust continuum and CN emissions are correlated with each other toward several star-forming regions. P. Hily-Blant et al. (2008) have shown a tight correlation between 1.3 mm dust and CN emissions. However, the number of their targeted regions was limited to only two low-mass prestellar cores, L1544 and L184. Examining the correlation with the more-increased number of samples in various star-forming regions would be necessary in order to increase the measurement reliability of the 3D magnetic field strength obtained from combining POS and LOS components of magnetic fields.

Here, we present the results of our study for the correlation between CN line and dust continuum emission in six high-mass star-forming regions, W3OH, OMC-1, NGC 2024, Mon R2, DR21, and S140. We selected the target sources from E. Falgarone et al. (2008), where CN Zeeman splitting lines were detected at their one or two positions except for Mon R2 where there is no CN Zeeman observation reported yet. In our study, we made CN line observations over all six targets using the 14 m telescope at the Taeduk Radio Astronomy Observatory (TRAO). We estimated CN and H₂ column densities using the CN integrated intensities and Herschel dust emission at 160, 250, 350, and 500 μm to compare their distribution, finding that there is a fairly good correlation between CN and dust emission. This result ensures the credibility of the estimation of 3D magnetic field strengths by combining dust polarization and CN Zeeman line observations. In our paper we give the 3D magnetic field strengths for our five high-mass star-forming regions, except for Mon R2.

This paper is organized as follows. In Section 2, we describe how we selected the six target sources and obtained the CN line and dust continuum data toward them. We explain in Section 3 how CN and H₂ column density maps are constructed. Then we discuss in Section 4 the similarity between the distributions of CN and dust emissions with their peak column density positions, a correlation between CN and H₂ column densities, and the 3D magnetic field strengths and their related mass-to-flux ratios in five high-mass star-forming regions. Our conclusions are given in Section 5.

2. Observations and Data Reductions

2.1. Targets

As observing targets, we selected five massive star-forming regions for which CN Zeeman observations have been made toward one or two positions with the Institut de Radio-astronomie Millimétrique (IRAM) 30 m telescope for measuring the line-of-sight strengths of the magnetic fields (Table 1; E. Falgarone et al. 2008). We included Mon R2 in our target list, although its CN Zeeman effect has not been observed yet, because it is expected to show a strong CN line emission from its strong submillimeter continuum emission as a nearby high-mass star-forming region (J. Hwang et al. 2022) and can be a good candidate for the future CN Zeeman measurement. The

information on our observing targets is listed in Table 1. The detailed information of each target is described in Appendix A.

2.2. Observations with TRAO 14 m Telescope

We carried out observations of CN ($N=1 \rightarrow 0$) spectral lines toward six high-mass star-forming regions using TRAO 14 m telescope located in Daejeon, South Korea,⁴ from 2018 October to November with the on-the-fly (OTF) mapping mode by using a receiver array system, a so-called the Second Quabbin Optical Image Array (SEQUOIA) equipped with a 4×4 MMIC preamplifiers. Two intermediate frequency (IF) modules allow us to observe two subbands in the frequency ranges of 85 and 100 GHz, or 100 and 115 GHz, simultaneously. The backend system provides each band to have 4096 channels with a resolution of 15 kHz and a bandwidth of 62.5 MHz. The beam efficiencies are 0.48 and 0.46 at 90 and 110 GHz, respectively (I.-G. Jeong et al. 2019).

The CN ($N=1 \rightarrow 0$) spectral lines have nine hyperfine structures (HFS). Our observations were simultaneously made for seven components out of them (Table 2) using two IF modules whose center frequencies are 113.17495 and 113.49097 GHz, respectively. The former and latter frequencies were tuned to observe the first three lines in Table 2 using the first IF module and the remaining four lines using the second IF module. Mapping observations were made over areas of either $6' \times 6'$ or $10' \times 10'$ in the six high-mass star-forming regions (Table 1). The center positions of mapping regions are listed in Table 1. The system temperatures vary from 320 to 540 K during our observations. The beam size of the TRAO is $46''$ at 113 GHz band. Our observing data were reconstructed with the Nyquist sampling of a pixel size of $22''$ and a spectral resolution of 0.3 km s^{-1} . The observation time spent for each source is either 60 or 100 minutes for the mapping size of $6' \times 6'$ or $10' \times 10'$, respectively. We made at least four OTF scan observations for each target and then averaged all OTF scans to get one averaged map. The line data analysis was performed using Continuum and Line Analysis Single-dish Software (CLASS; J. Pety 2005; T. Gildas 2013).⁵ All seven hyperfine components of CN in the observing frequency range toward six targets were strongly detected with a high signal-to-noise ratio (S/N) > 10 for the brightest component at their peak intensity positions. The mean brightness temperatures of the sixth hyperfine component at 113.49964 GHz used in our analysis are found to range from 0.17 to 0.54 K in our targets, with the mean rms temperatures of $0.04 \sim 0.08$ K. Figure 1 shows the CN spectra of all targets at the OTF map central positions given in Table 1. We smoothed each spectrum in the velocity domain to have its resolution of 0.6 km s^{-1} . The peak values of the spectra are shown in Table 1.

Figure 2 shows the integrated intensity maps for the sixth CN hyperfine component, as the optically thinnest component of the seven ones, toward the six target sources where the intensity is integrated into the velocity ranges listed in Table 1. The temperature in the maps is given in the scale of the main beam temperature (T_R) by considering the beam efficiency (46%) of TRAO at 110 GHz.

⁴ <https://trao.kasi.re.kr>

⁵ <https://www.iram.fr/IRAMFR/GILDAS>

Table 1
Observed Targets

(1) Source Name	(2) R.A. (J2000)	(3) Decl. (J2000)	(4) Mapping Size ($' \times '$)	(5) v_{LSR} (km s^{-1})	(6) T_A^* (K)	(7) σ_{CN} (K km s^{-1})	(8) Δv ($\text{km s}^{-1}, \text{km s}^{-1}$)	(9) d (kpc)
W3OH	02:27:04.1	61:52:22	10×10	-48.1	0.3	0.13	[-54, -39]	$2.00^{+0.29}_{-0.23}$
OMC-1	05:35:14.5	-05:22:07	10×10	8.3	0.8	0.27	[2, 17]	0.39 ± 0.01
NGC 2024	05:41:44.2	-01:55:41	10×10	11.0	1.1	0.31	[3, 18]	0.36 ± 0.02
Mon R2	06:07:46.0	-06:22:45	10×10	9.8	0.4	0.14	[3, 17]	0.78 ± 0.04
DR21	20:38:59.9	42:22:38	6×6	1.8	-3.6	0.5	[-7, 7]	$1.40^{+0.12}_{-0.11}$
S140	22:19:17.1	63:18:35	6×6	-7.2	1.5	0.5	[-12, 2]	0.91 ± 0.01

Note. Columns: (1) Name of source; (2) and (3) R.A. and decl. of the central position of the CN line on-the-fly (OTF) map, where the CN Zeeman observations have been made (E. Falgarone et al. 2008); (4) the OTF mapping size for the TRAO observations; (5) LSR velocity of CN sixth hyperfine component at the OTF mapping center; (6) the peak antenna temperature of the sixth hyperfine component of the CN line at the OTF mapping center; (7) the rms value of CN integrated intensity; (8) the velocity range for the integrated intensity map for the sixth hyperfine component of the CN line in Figure 2; (9) the distance of the target. The references are given in Appendix A.

Table 2
CN ($N = 1 \rightarrow 0$) Hyperfine Transitions

(1) Line	(2) Transition $N, J, F \rightarrow N', J', F'$	(3) Frequency (GHz)	(4) Relative Intensity
1	$1, 1/2, 1/2 \rightarrow 0, 1/2, 3/2$	113.14416	8
2	$1, 1/2, 3/2 \rightarrow 0, 1/2, 1/2$	113.17049	8
3	$1, 1/2, 3/2 \rightarrow 0, 1/2, 3/2$	113.19128	10
4	$1, 3/2, 3/2 \rightarrow 0, 1/2, 1/2$	113.48812	10
5	$1, 3/2, 5/2 \rightarrow 0, 1/2, 3/2$	113.49097	27
6	$1, 3/2, 1/2 \rightarrow 0, 1/2, 1/2$	113.49964	8
7	$1, 3/2, 3/2 \rightarrow 0, 1/2, 3/2$	113.50891	8

2.3. Herschel Data

We used dust continuum data obtained from the Herschel Space Observatory to get H_2 column density maps in order to compare them with CN column density maps. The data for all the targets were retrieved from the Herschel archive. The Herschel is equipped with two photometric instruments, Photodetector Array Camera and Spectrometer (PACS; A. Poglitsch et al. 2010) and a Spectral and Photometric Imaging REceiver (SPIRE; M. J. Griffin et al. 2010), which enables to observe a field in five photometric bands at 70, 160, 250, 350, and 500 μm . The beam sizes of the Herschel are $5''$, $11''$, $18''$, $25''$ and $36''$ at 70, 160, 250, 350, and 500 μm , respectively. The continuum images at 160, 250, 350, and 500 μm for six targets were cropped to have the same sizes as the ones of CN maps in each target (Table 1). The observation Identity Documents (IDs) of the data are 1342189702, 1342218967, 1342215984, 1342204052, 1342186840, and 1342187331 for W3OH, OMC-1, NGC 2024, Mon R2, DR21 and S140, respectively.

2.4. JCMT Data

The dust polarization data of the targets were retrieved from the data archive of the James Clerk Maxwell Telescope (JCMT) observatory. The polarization data for all targets except for S140 were obtained from observations by a polarimeter POL-2 (P. Friberg et al. 2016) inserted in the Submillimeter Common-User Bolometer Array 2 (SCUBA-2; W. S. Holland et al. 2013) camera, while the dust polarization data for S140 were taken using the previous polarimeter the

JCMT, the SCUPOL. Project codes of the Pol-2 data used in this paper are M16AL004 (OMC-1; P.I.: Derek Ward-Thompson), M17BL011 (Mon R2, DR21; P.I.: Derek Ward-Thompson), M21BP020 (NGC 2024; P.I.: Nicolas Peretto), and E21BJ002 (W3OH; P.I.: Shu-ichiro Inutsuka). The S140 data were obtained from the SCUPOL legacy catalog (B. C. Matthews et al. 2009).

3. Results

3.1. Distribution of CN Line Emission and Herschel Continuum Emission

Figure 3 compares CN line emission in contours with dust continuum emission in color tones for six targets, indicating that the regions emitting CN emission are well matched with those emitting dust emission. Especially, the peak CN and dust intensities are very well correlated, indicating that the CN and dust emission may be coming from the similarly high density regions. We attempt to examine at which column density level the CN line and dust continuum would similarly emit in the dense regions. For this purpose, we estimate CN column density using our CN observations and H_2 column density using the Herschel data in Sections 3.2 and 3.3 and examine their distribution features in Section 4.

3.2. CN Column Density

The CN column density can be estimated from the following equation derived with optically thin and the Rayleigh-Jeans approximation ($h\nu \ll kT_{\text{ex}}$ at 113 GHz; J. G. Mangum & Y. L. Shirley 2015),

$$N_{\text{CN}} = \left(\frac{3k}{8\pi^3 S \mu_0^2 R_i} \right) \left(\frac{Q_{\text{rot}}}{g_J g_K g_I} \right) \exp\left(\frac{E_u}{kT_{\text{ex}}} \right) \int \frac{T_R T_{\text{ex}}}{f(T_{\text{ex}} - T_{\text{bg}})} dv, \quad (1)$$

where k is the Boltzmann constant, S is the line strength, μ_0 is the dipole moment, R_i is the relative strength of all transitions, $Q_{\text{rot}} = kT_{\text{ex}}/hB_0 + 1/3$ is the rotational partition function that represents a statistical sum over all rotational energy levels in the molecule, h is Planck's constant, B_0 is the rigid rotor rotation constant, T_{ex} is the excitation temperature, E_u is the energy in upper level u , g_J is the rotational degeneracy, g_K is the K degeneracy associated with the internal quantum number

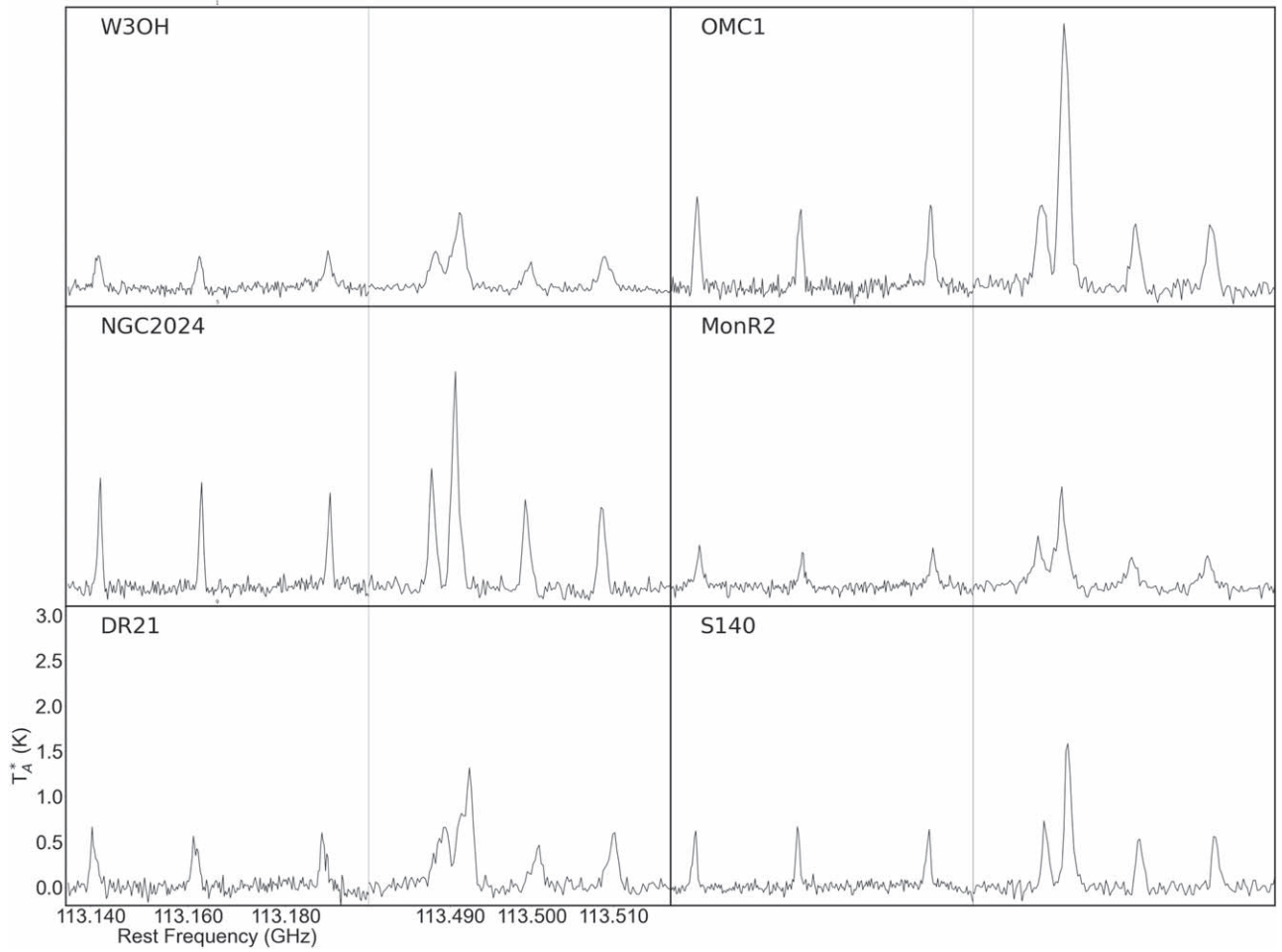


Figure 1. CN ($N = 1 \rightarrow 0$) spectra toward the center positions of the OTF maps for each target (Table 1). In each panel a thin solid line divides the seven hyperfine lines into two groups; one group of three lines with energy level transitions of $N = 1 \rightarrow 0$, $J = 1/2 \rightarrow 1/2$ and another group of four lines with the transitions of $J = 3/2 \rightarrow 1/2$.

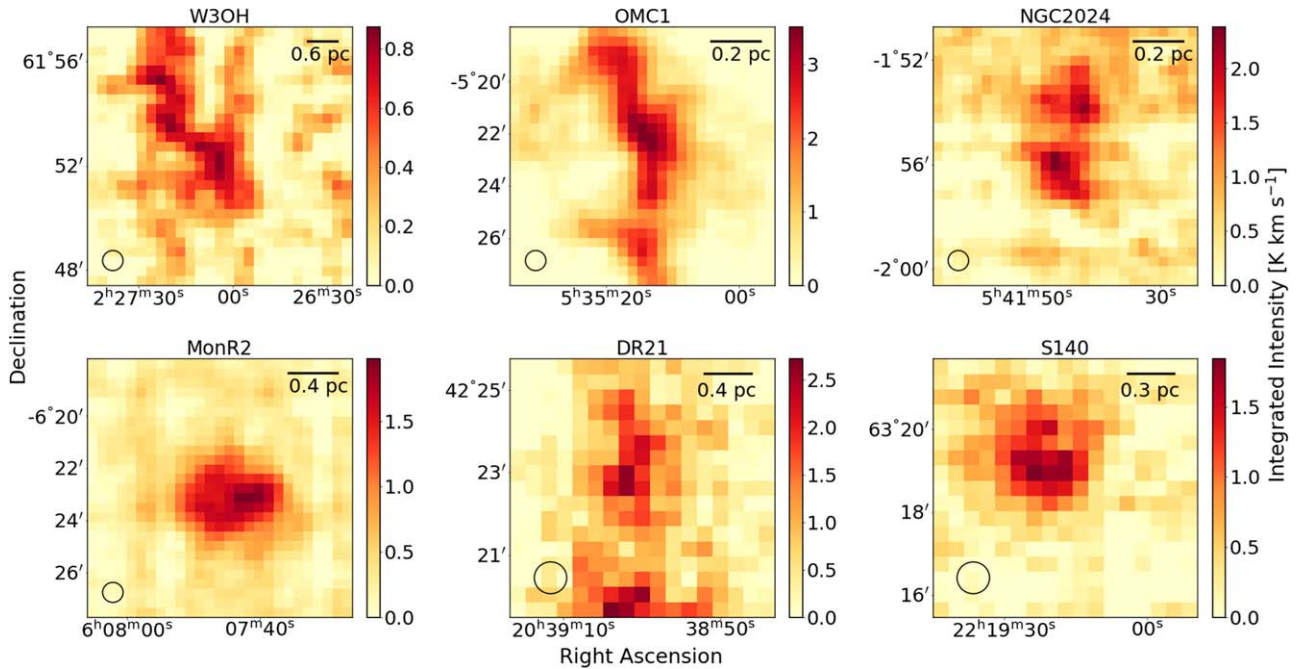


Figure 2. Integrated intensity maps of the sixth CN hyperfine transition toward the target sources. A circle in the lower left corner of each panel shows the beam size ($46''$) of the TRAO 14 m telescope. The velocity range for the intensity integration for each map is listed in Table 1.

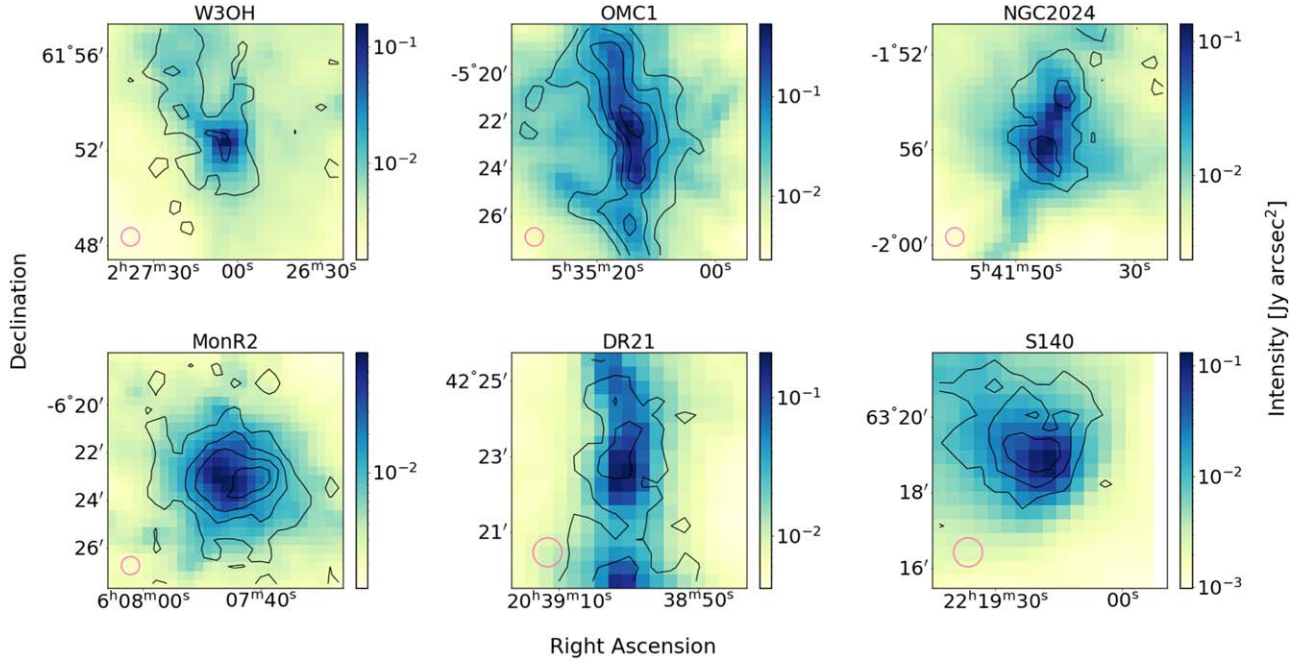


Figure 3. Color images of dust continuum obtained with Herschel at $500\ \mu\text{m}$. The Herschel images are convolved to the TRAO beam size, $46''$, which is marked as a pink circle in the lower left corner. Contours indicate the distribution of CN integrated intensities from $3\sigma_{\text{CN}}$ in steps of $3\sigma_{\text{CN}}$ where the σ_{CN} is the uncertainty of CN integrated intensity in a unit of K km s^{-1} listed in Table 1.

K , g_I is the nuclear spin degeneracy, T_{bg} is the background temperature assumed to be $2.7\ \text{K}$ as the cosmic microwave background temperature (D. J. Fixsen 2009), f is the filling factor assumed as a unit, and $\int T_R d\nu$ is the integrated intensity of the CN emission. For the estimation of the CN column density, we used the sixth hyperfine component of CN ($N, J, F \rightarrow N', J', F' = 1, 3/2, 1/2 \rightarrow 0, 1/2, 1/2$), which has the least optical depth among the seven HFS components. We used $\mu_0 = 1.45$ Debye, $E_u = 5.45\ \text{K}$, and $B_0 = 56693.47\ \text{MHz}$ given by the Jet Propulsion Laboratory (JPL) molecular spectroscopy database⁶ and spectral line catalog (H. M. Pickett et al. 1998). The Q_{rot} is given as $0.37(T_{\text{ex}} + 0.9)$ for the sixth transition of CN. The derivation of the excitation temperature using CN hyperfine lines is found to be not straightforward, usually suffering from a large degeneracy in its determined values, especially in the optically thin case of the CN line. Therefore we used the dust temperature as the excitation temperature by assuming that the CN and dust are well mixed. In fact, Figure 3 shows that distributions of CN and dust emission are well matched at least around their emission peak regions, and thus using the dust temperatures toward the emission peak regions is thought to be viable. Figure 4 shows the maps of the estimated CN column density. A more detailed comparison between CN and H_2 column densities in each region is given in Section 4.2.

3.3. H_2 Column Density

The H_2 column density can be estimated by combining the Herschel 160, 250, 350, and $500\ \mu\text{m}$ data. The spectral energy distribution (SED) of the Herschel data is used to estimate the dust temperature, and the $500\ \mu\text{m}$ data are used to derive the H_2 column density with an assumption of a gas-to-dust mass ratio

of 100. The equation for the estimation of the H_2 column density is given as follows,

$$N_{\text{H}_2} = \frac{I_\nu}{\mu m_{\text{H}} \kappa(\nu) B_\nu(T)}, \quad (2)$$

where I_ν is the intensity at the frequency ν (R. H. Hildebrand & 1983), $B_\nu(T)$ is the Planck function at dust temperature T , $\mu = 2.8$ is the mean molecular weight per hydrogen molecule (J. M. Kirk et al. 2013), m_{H} is the mass of a hydrogen atom, $\kappa(\nu) = \kappa_{\nu_0} (\nu/\nu_0)^\beta$ is the dust opacity function where $\kappa_{\nu_0} = 0.1\ \text{cm}^2\ \text{g}^{-1}$ at $\nu_0 = 1000\ \text{GHz}$ (F. Motte & P. André 2001; P. André et al. 2010), and $\beta = 2$ is the dust emissivity index (S. V. W. Beckwith et al. 1990).

We determined the dust temperature and H_2 column density for the targets using the above equation through an iterative SED fitting of the Herschel data at 160, 250, 350, and $500\ \mu\text{m}$, starting from an initial guess of the column density as $10^{22}\ \text{cm}^{-2}$. Note that before the SED fitting procedure, we subtracted the background emission at regions about $9''$ – $10''$ away from the central position of each map to remove any possible emission contribution from the Galactic plane in the targets. Then, we convolved the 160, 250, and $350\ \mu\text{m}$ data in a different beam size to have a beam size of $500\ \mu\text{m}$ data, $36''$, and aligned data pixels at 160, 250, and $350\ \mu\text{m}$ to the coordinates for $500\ \mu\text{m}$ data. Then we obtain the best-fit dust temperature giving the lowest χ^2 value from the SED fit using a Python package of *curve_fit* and estimate H_2 column density with this dust temperature using $500\ \mu\text{m}$ data. The estimated column density is again used for the next round of the SED fit to determine an improved dust temperature, with which the column density is again estimated. The fitting range of temperature was assigned from 2.7 to 100 K. This iteration of the SED fit continues until the reestimated H_2 column density agrees within 1% of its previous value. We chose $500\ \mu\text{m}$ data in the fit and in the calculation of the H_2 column density. This is mainly because the beam size of the $500\ \mu\text{m}$ data is closer to

⁶ <https://spec.jpl.nasa.gov/ftp/pub/catalog/catdir.html>

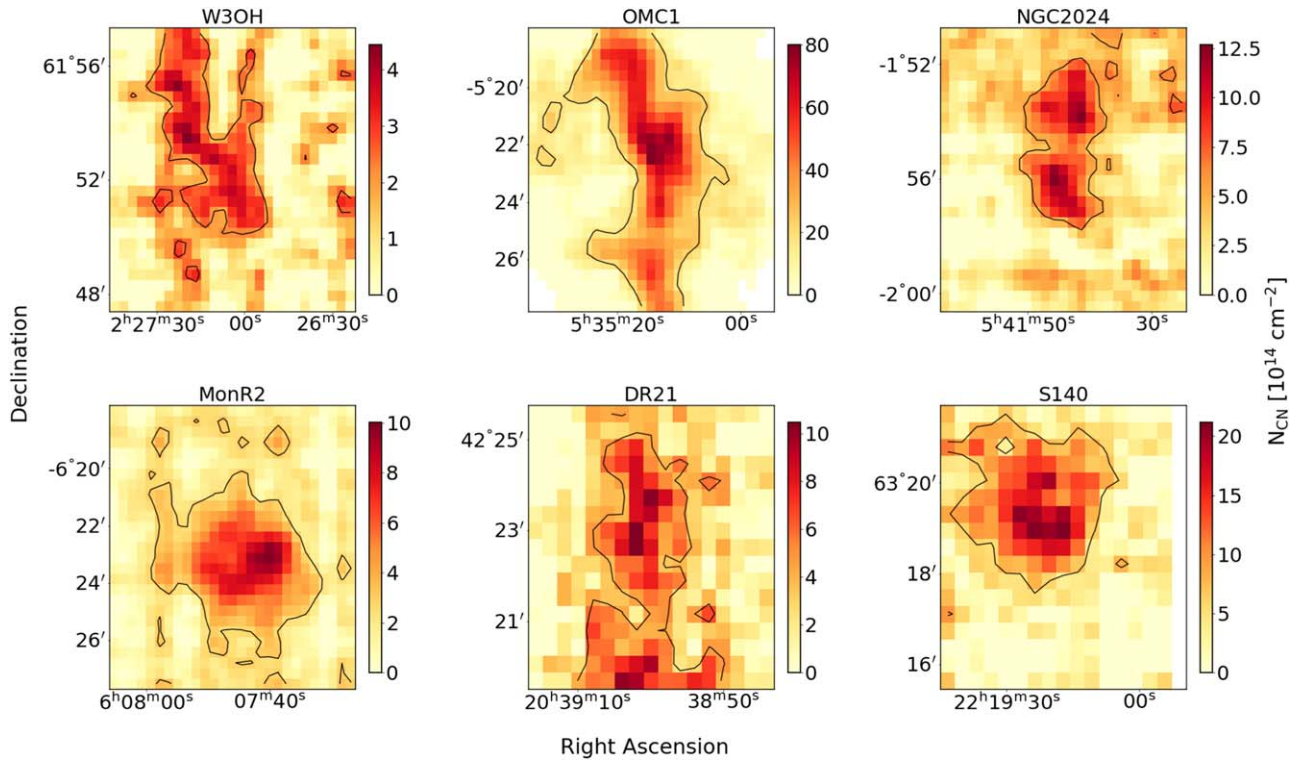


Figure 4. Maps of CN column density of the target sources. Black contours in each panel delineate a $3\sigma_{\text{CN}}$ level.

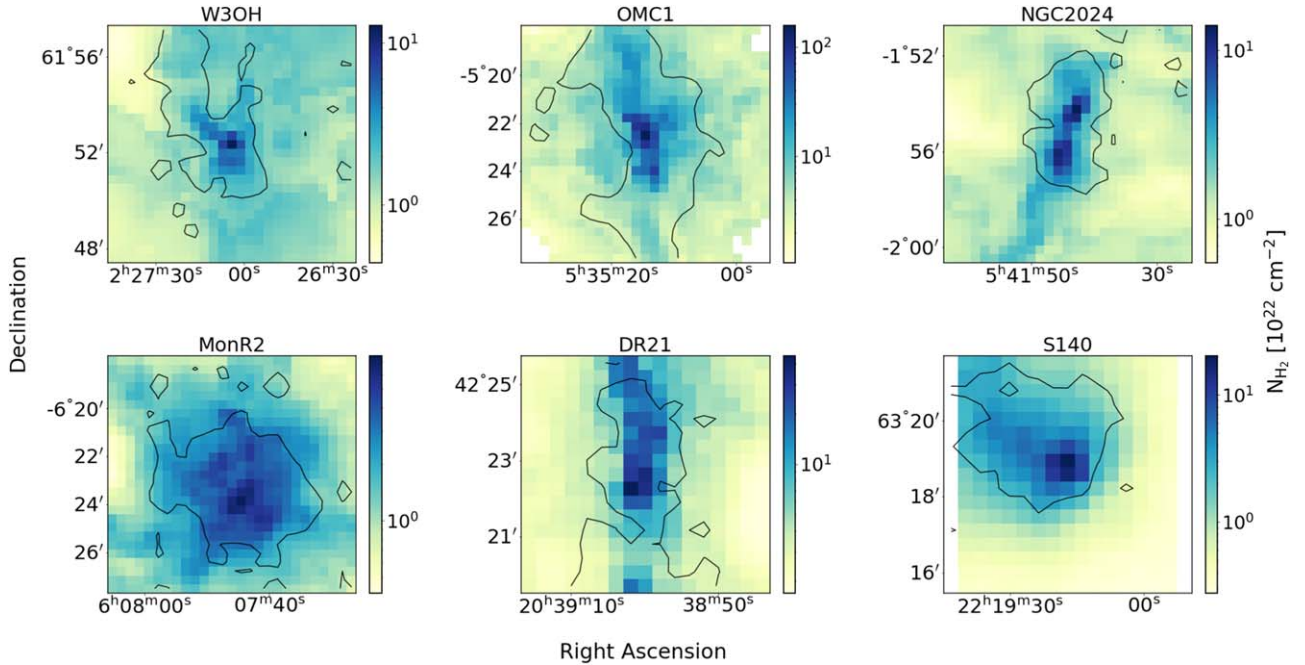


Figure 5. Maps of the H_2 column density of the target sources. The column density is estimated by the SED fitting procedure of the Herschel data at four wavelengths. Black contours indicate the $3\sigma_{\text{CN}}$ level.

the beam size of the TRAO data (CN line data) than those for 350 and 250 μm data. We have also used dust continuum data at 350 and 250 μm data in deriving the H_2 column densities, finding the derived H_2 column densities are consistent with the values obtained using 500 μm data within 5% of the values from 500 μm data in their differences.

In this way, we determined the H_2 column densities and dust temperatures in all pixels of all targets. The obtained H_2

column density maps are shown in Figure 5. In the case of S140, there are no PACS observations at 160 μm , so we used the data at 250, 350, and 500 μm for the SED fitting. In SPIRE observations, bright sources can be saturated, and so these sources are usually set to be observed in the bright mode.⁷ However, S140 has not been observed with this bright mode. In

⁷ http://herschel.esac.esa.int/Docs/SPIRE/pdf/spire_om_v24.pdf

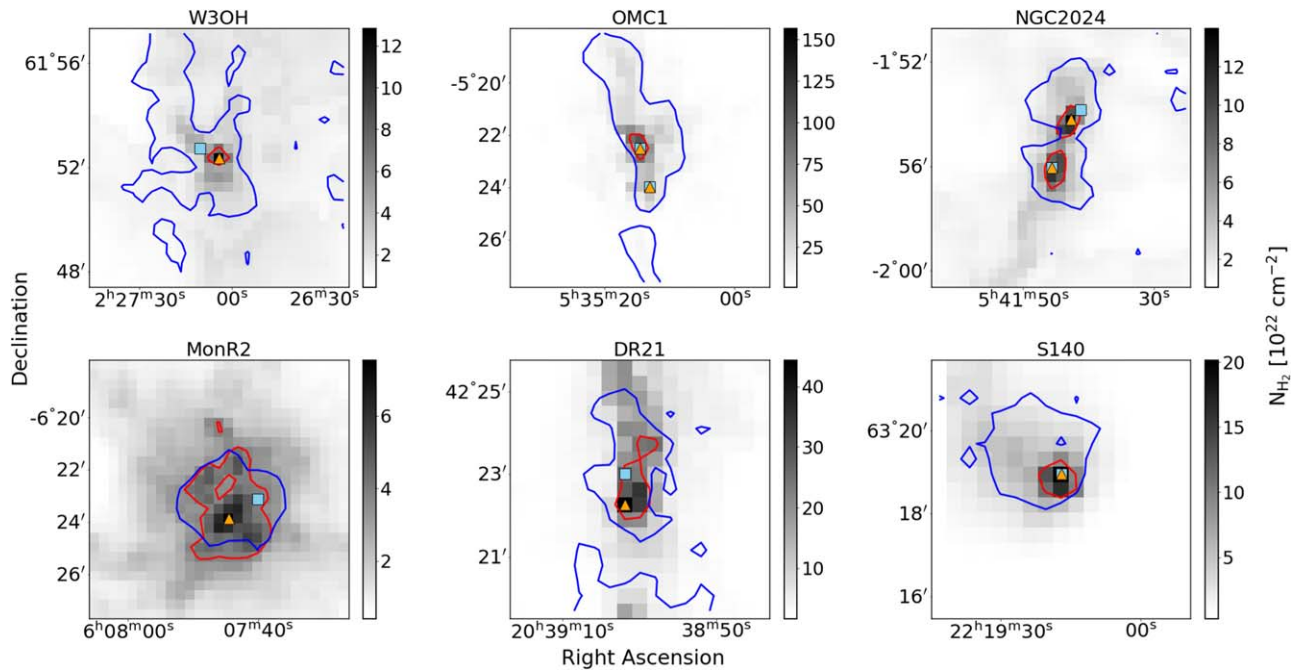


Figure 6. The spatial distribution of the CN and H₂ column densities. A gray image displays the distribution of the H₂ column density. The scale bar in each panel indicates the value of the column density. Blue and red contours in each panel delineate the half-maximum levels of CN and H₂ column densities, respectively. Cyan squares and orange triangles indicate the peak positions for CN and H₂ column densities, respectively. OMC-1 and NGC 2024 show two sets of symbols for local column density peaks for two clumps for each source.

a few central pixels of S140, there are no values at 250 μm because of the intensity saturation issue. In this case, we used the highest value at 250 μm at a pixel nearby from those pixels for the SED fitting. In the case of OMC-1, a few pixels of dust continuum at 160 μm are also found to be saturated, having no values assigned. In this case, we used the data at 250, 350, and 500 μm data for the SED fitting.

4. Discussions

This section discusses how CN- and dust-emitting regions are spatially related. For this purpose, we examine how peak positions and half-maximum (HM) contours are coincident and how well CN- and dust-emitting regions are physically related. Here the HM contours are meant to be the contours having half values of the peak CN and H₂ column densities in their column density distribution. From the likely spatial coincidence between CN and dust emissions, the possible 3D magnetic field strengths are estimated in five high-mass star-forming regions, and how their measurements would affect the physical status of the star-forming regions is discussed. For the direct comparison of two column densities, the H₂ column density maps derived with Herschel continuum emission were convolved to the TRAO beam size and regridded to fit the pixels of the CN column density maps.

4.1. Spatial Relation between CN-line- and Dust-continuum-emitting Regions

CN line emission has been detected in star-forming regions with densities ranging from 10^4 to 10^6 cm^{-3} (B. E. Turner & R. H. Gammon 1975), where there are dense cores that may start to collapse to form stars. However, it has been questionable whether the CN emission showing the Zeeman effect comes from the central regions of the dense cores that

can be well traced with dust continuum emission. Therefore, it is necessary to make a systematic comparison between the peak positions of CN and dust emission.

Here we make a similar comparison for CN and H₂ column density maps for the six high-mass star-forming regions in Figure 6. The main purpose of the comparison is to examine how the CN line bright regions are closely related to dust continuum bright regions, and thus we added two more peak intensity positions in OMC-1 and NGC 2024 showing multiple local peak intensity positions in CN and dust intensity distribution. Therefore we were able to consider eight strong intensity positions in comparing the peak positions of CN-line- and dust-continuum-emitting regions, finding that the peak positions of CN column densities in the targets are closely located to the peak positions of H₂ column densities. The separations of the peak positions are within or less than the beam size of the TRAO, $\sim 46''$, except for Mon R2 whose separation is $\sim 79''$ (see Figure 7).

We also examine the features of CN line and dust emission distributions by comparing the HM contour areas of CN and H₂ column density maps (Figure 6). We find that the HM contour areas of CN column density maps are usually wider, by at least 7 times, than those of the H₂ column density maps in all targets, except for Mon R2 where such areas of CN and H₂ column densities are comparable. However, we note that the areas of $> 5\sigma$ level are wider in the H₂ column density maps than in CN column density maps because of the superior sensitivity in dust continuum data (Appendix B), indicating that CN emission is more widely distributed in the dense core regions than the dust continuum emission while dust continuum emission traces more extended area in the low-density regions.

In summary, CN emission is usually bright at the dust continuum bright region, tracing a more extended area than the dust-emitting area in the dense core regions. Dust continuum

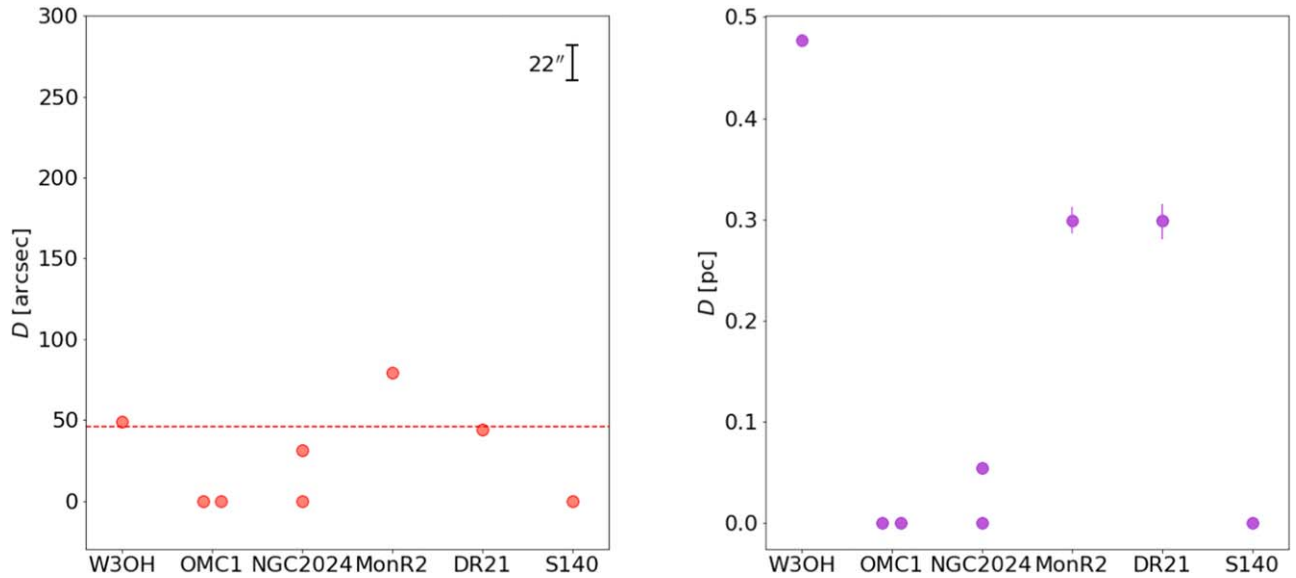


Figure 7. The spatial separations between peak positions in CN and H_2 column density distributions for the observing targets, in units of arcsec (left) and parsec (right). The dashed red line in the left panel indicates the TRAO beam size of $46''$. A bar for the pixel size of $22''$ is shown in the upper-right corner of the left panel. The error bars shown in the right panel are estimated from the distance uncertainties of the target sources listed in Table 1.

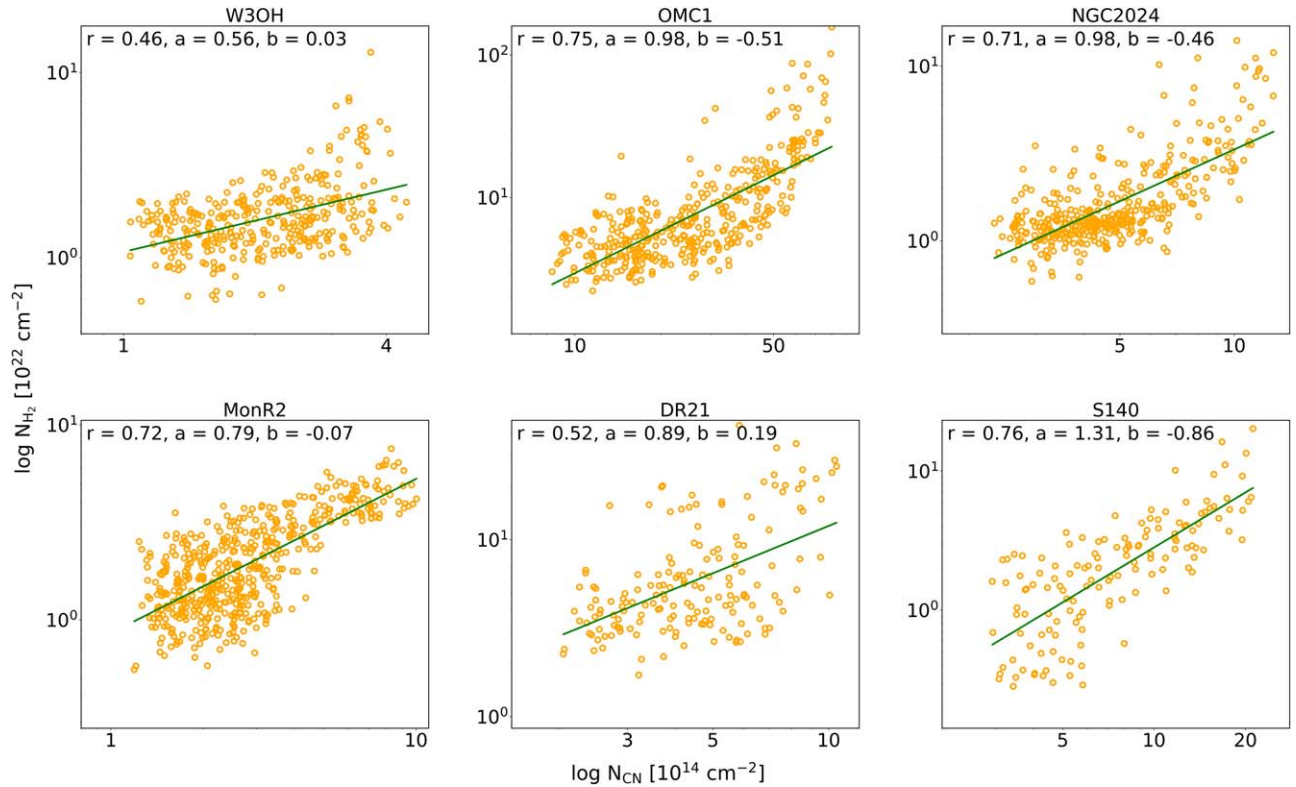


Figure 8. Correlation between column densities of CN and dust toward six target sources. A green line in each panel draws a best-fitting result of both column densities with a function, $\log N_d = a \log N_{CN} + b$. The correlation coefficient, r , and the fitting parameters, a and b , are given at the upper part of each panel.

data are more sensitive enough to trace the low-density extended area than CN emission data.

4.2. Correlation between CN and H_2 Column Densities

How CN-line-emitting regions relate to the dust-continuum-emitting regions can also be examined with the correlation between CN and H_2 column densities toward the targets, as shown in Figure 8. The figure plots two column densities

within regions enclosed by $3\sigma_{CN}$ level (Figure 4) for which the H_2 column densities are at least larger than $1.6 \times 10^{21} \text{ cm}^{-2}$. The correlation coefficients r between both column densities are larger than 0.7 in four targets, indicating a good correlation between two column densities in those sources. In the case of two targets, W3OH and DR21, the correlation coefficients are 0.46 and 0.52, respectively, meaning that the correlation between two column densities in two targets is not as tight as those for the other four targets. Even in this case, however, we

Table 3
Parameters for Estimating the POS Component of the Magnetic Field by the DCF Method

(1) Source	(2) σ_θ (deg)	(3) σ_v (km s ⁻¹)	(4) N_{H_2} (10 ²² cm ⁻²)	(5) R_{eff} (pc)	(6) n_{H_2} (10 ⁴ cm ⁻³)
W3OH	39 ± 2.9	1.5 ± 0.6	12.8 ± 0.2	0.24	8.6 ± 0.2
OMC-1	10.2 ± 0.1	1.3 ± 0.7	87.3 ± 8.7	0.05	302.9 ± 30.0
NGC 2024	19.9 ± 1.6	1.1 ± 0.3	9.9 ± 0.2	0.07	21.4 ± 0.3
Mon R2	21.7 ± 1.9	1.9 ± 0.7	3.6 ± 0.1	0.39	1.5 ± 0.03
DR21	5.9 ± 0.3	1.7 ± 0.7	35.0 ± 0.7	0.24	23.8 ± 0.6
S140	10.6 ± 7.5	1.0 ± 0.4	16.2 ± 1.0	0.12	21.5 ± 1.3

Note. Columns: (1) Source name; (2) polarization angle dispersion obtained using SCUPOL and POL-2 observations from the JCMT (see Section 2.4); (3) velocity dispersion of CN sixth hyperfine line obtained at the position where CN Zeeman effect has been detected; (4) H₂ column density; (5) effective radius for the area within the HM contour of the H₂ column density map; (6) volume density obtained by dividing the column density with twice the effective radius.

note that two CN and H₂ column densities are positively correlated in the sense that the CN column densities get higher at the high H₂ column density regions.

4.3. 3D Magnetic Field Strength

In Sections 4.1–4.2, we found that CN column densities are positively correlated with H₂ column densities in the targets. In particular, the spatial positions showing the peak column density of CN are even better correlated with the positions showing the peak H₂ column density within one or two TRAO beam sizes in all targets, while the CN-emitting area is more extended than the dust-emitting area in the dense core regions. From this, we see a reliability of combining both LOS and POS components of magnetic field strengths (B_{LOS} and B_{POS}) measured in the high dense regions to obtain 3D magnetic field strengths of our targets as these two CN line and dust continuum emissions are likely coming from a spatially similar area especially in the dense central regions of the clouds with at least over the H₂ column density of 8.0×10^{22} cm⁻². Therefore, we attempt to estimate the 3D magnetic field strengths toward our targets by making a vector sum of two LOS and POS components of the magnetic fields that have been measured for these targets and discuss the role of the magnetic field in the star formation activity in the targets using their 3D magnetic field strengths. The B_{LOS} in Mon R2 has not been obtained, and thus its 3D magnetic field strength could not be estimated.

The LOS magnetic field strengths have been obtained by the CN Zeeman effect toward a single position of the targets using the IRAM 30 m telescope with a beam size of 24'' (E. Falgarone et al. 2008). However, the POS magnetic field strengths for each target were not necessarily estimated toward the position where the LOS component is measured, but usually given as mean values over the targets (see Appendix A). Therefore we reestimated the POS magnetic field strengths in each target toward the positions where the LOS magnetic field strengths were measured, using the following equation (R. M. Crutcher et al. 2004),

$$B_{\text{POS}} \approx 9.3 \sqrt{n(\text{H}_2) [\text{cm}^{-3}]} \frac{\Delta V [\text{kms}^{-1}]}{\sigma_\theta [\text{degree}]}, \quad (3)$$

where n_{H_2} is the volume density of molecular hydrogen, $\Delta V = 2\sqrt{2} \ln 2 \sigma_v$ is the full width at half-maximum of the nonthermal component of a spectral line, σ_v is the velocity dispersion of the nonthermal gas component, and σ_θ is the

polarization angle dispersion. The volume density was estimated by dividing the column density of H₂ width by a cloud depth, which is given here as an effective radius of $R_{\text{eff}} = \sqrt{A/\pi}$, where A is the area within the HM contour of the H₂ column density map. The estimated H₂ volume densities for six targets are listed in Table 3, which are consistent with those determined from other line observations for the same targets within a few factors (E. Falgarone et al. 2008). The σ_v was estimated from the CN line profile obtained from our TRAO observations using $\sigma_v = \sqrt{\sigma_{\text{obs}}^2 - kT_k/m_{\text{CN}}}$, where σ_{obs} is obtained by the Gaussian fit for the sixth hyperfine component of CN, T_k is the kinetic temperature, which is assumed to be the same as the dust temperature, and m_{CN} is the mass of the CN molecule.

Polarization angle dispersion (σ_θ) was derived by using a new technique in the DCF method by J. Hwang et al. (2021) in which field strengths are measured in a moving box with a small size where any curvature of magnetic field line would not affect the estimation of the field strength. In our measurement of polarization angle dispersion for deriving the POS component of the magnetic field strength, the box size was chosen as small as possible to best fit to the beam size of 24'' with which the LOS component was measured. By using dust polarization maps obtained by the POL-2 or SCUPOL on the JCMT (B. C. Matthews et al. 2009; J. Hwang et al. 2021, 2022), we binned the polarization segments with a pixel size of 12'', chose a box of 3 × 3 pixels containing nine polarization segments, and reestimated polarization angle dispersion in the box. It turned out that a box size of 3 × 3 pixels corresponding to the beam size of 36'' is significantly smaller than the radius of magnetic field curvature, making the polarization angle dispersion smaller than 25° in most cases and thus the measurement of POS strength of the magnetic field to be reliable. The POS magnetic field strengths and other physical parameters used for the DCF method for each source are listed in Table 4.

We simply took vector sums of the POS and LOS components of five target sources to estimate their 3D magnetic field strengths (B ; Table 4), which range from 0.6 to 4.9 mG and thus drove the mass-to-flux ratios for our targets that can be useful for discussing on the relative importance of magnetic fields in their star-forming activities. A dimensionless mass-to-flux ratio (λ) is given by dividing its observed value by the critical value in a magnetized disk structure (T. Nakano &

Table 4
Magnetic Field Strengths and Mass-to-flux Ratios

(1) Source	(2) B_{LOS} (mG)	(3) B_{POS} (mG)	(4) $B_{\text{POS,cor}}$ (mG)	(5) B (mG)	(6) B_{cor} (mG)	(7) λ	(8) λ_{cor}
W3OH	1.10 ± 0.33	0.3 ± 0.1	0.08 ± 0.03	1.1 ± 0.3	1.10 ± 0.33	0.9 ± 0.2	0.9 ± 0.3
OMC-1	-0.36 ± 0.08	4.9 ± 2.6	1.23 ± 0.65	4.9 ± 2.6	1.28 ± 0.62	1.4 ± 0.7	5.2 ± 2.6
NGC 2024	0.01 ± 0.12	0.6 ± 0.2	0.11 ± 0.05	0.6 ± 0.2	0.15 ± 0.05	1.2 ± 0.4	5.0 ± 1.7
Mon R2	...	0.6 ± 0.2	0.05 ± 0.03
DR21	-0.54 ± 0.11	3.1 ± 1.3	0.78 ± 0.33	3.1 ± 1.3	0.94 ± 0.29	0.8 ± 0.3	2.8 ± 0.8
S140	-0.25 ± 0.09	1.0 ± 0.8	0.25 ± 0.20	1.0 ± 0.8	0.35 ± 0.16	1.2 ± 0.9	3.5 ± 1.5

Note. Columns: (1) Source name; (2) LOS magnetic field strength obtained with CN Zeeman observations (E. Falgarone et al. 2008). In the case of DR21, a mean value of two measurements is given; (3) POS magnetic field strength by the DCF method obtained using parameters listed in Table 3; (4) POS magnetic field strength reduced by a statistical factor of 4; (5) 3D magnetic field strength by a vector sum of two values in columns (2) and (3); (6) 3D magnetic field strength by a vector sum of the POS and the LOS values in columns (2) and (4); (7) mass-to-flux ratio by the values in column (5) and H_2 column density; (8) mass-to-flux ratio by the values in column (6) and H_2 column density.

T. Nakamura 1978; R. M. Crutcher et al. 2004),

$$\lambda = 7.6 \times 10^{-21} \frac{N_{\text{H}_2} [\text{cm}^{-2}]}{B [\mu\text{G}]} \quad (4)$$

This ratio was estimated using the H_2 column density in Table 3 and B in Table 4. A source for which λ is smaller than 1 is referred to be magnetically subcritical, implying that the magnetic field over the source is strong enough against its gravitational collapse, while the source for which λ is larger than 1 is magnetically supercritical, and in this case, the magnetic field is not strong enough to resist against the gravitational collapse over the source.

For making a more reasonable estimation for the 3D magnetic field strength and the mass-to-flux ratio, here we discuss possible statistical overestimation of the B_{POS} in comparison with the B_{LOS} . If 3D magnetic field vectors are randomly oriented, the angle-averaged mean POS and LOS components would be factors of $\pi/4 \sim 0.79$ and 0.5 smaller than the 3D magnetic field strength, respectively (T. Pillai et al. 2016), and thus the strength of POS component of any 3D magnetic field vector could be statistically $\pi/2 (=1.58)$ times larger than that of its LOS component. However, K. Pattle et al. (2023) showed that for all possible compilations of the observed sources, the POS magnetic field strengths measured by the DCF method are on average 6.3 ± 1.5 times larger than those obtained by Zeeman measurements. Then it is possible that the measurement of POS strength by the DCF method is statistically overestimated by a factor of $6.3/1.58 \sim 4$. Because of this, we corrected the POS magnetic field strength by dividing a factor of 4 to calculate the corrected 3D magnetic field strength (B_{cor}) for our targets. The mass-to-flux ratios (λ_{cor}) of our targets were estimated using this corrected 3D magnetic field strength, which ranges from 0.9 to 5.2. The estimated λ_{cor} values for our targets are all listed in Table 4, indicating that our sources are magnetically supercritical, except for W3OH, which is more likely in a magnetically transcritical status.

5. Summary

We carried out the observations of the CN $N = 1-0$ hyperfine transitions toward the six high-mass star-forming regions using the TRAO 14 m telescope to examine how the CN-emitting regions are coincident with the dust-emitting regions.

First of all, CN column densities are found to be positively correlated with H_2 column densities all over the targets, and in particular, the peak CN column density areas are even better correlated with the peak H_2 column density areas of the H_2 column density of $>8.0 \times 10^{22} \text{cm}^{-2}$ within one or two telescope beam size in all targets, indicating that CN-line- and dust-continuum-emitting regions are likely spatially coincident. This justifies making a vector sum of both LOS components (from the CN Zeeman effect observations) and POS components (from the dust polarization observations) of magnetic field strengths to obtain 3D magnetic field strengths toward the high column density regions of high-mass star-forming clouds.

By using this 3D magnetic field strength, the mass-to-flux ratios were estimated to examine the stability of our high-mass star-forming clouds, finding that the sources are magnetically supercritical or transcritical, and thus the magnetic field strengths in the sources may not be sufficient to support them against gravitational collapse.

Acknowledgments

This research was supported by the Korea Astronomy and Space Science Institute (KASI) under the Research and Development (R&D) program supervised by the Ministry of Science and ICT. The JCMT is operated by the East Asian Observatory on behalf of The National Astronomical Observatory of Japan; Academia Sinica Institute of Astronomy and Astrophysics; the Korea Astronomy and Space Science Institute; the Operation, Maintenance and Upgrading Fund for Astronomical Telescopes and Facility Instruments, budgeted from the Ministry of Finance of China. Additional funding support is provided by the Science and Technology Facilities Council of the United Kingdom and participating universities and organizations in the United Kingdom, Canada, and Ireland. Additional funds for the construction of SCUBA-2 were provided by the Canada Foundation for Innovation. The Herschel spacecraft was designed, built, tested, and launched under a contract to ESA managed by the Herschel/Planck Project team by an industrial consortium under the overall responsibility of the prime contractor Thales Alenia Space (Cannes), and including Astrium (Friedrichshafen) responsible for the payload module and for system testing at spacecraft level, Thales Alenia Space (Turin) responsible for the service module, and Astrium (Toulouse) responsible for the telescope,

with in excess of a hundred subcontractors. C.W.L. is supported by the Basic Science Research Program through the NRF funded by the Ministry of Education, Science and Technology (NRF-2019R1A2C1010851) and by the Korea Astronomy and Space Science Institute grant funded by the Korean government (MSIT; project No. 2024-1-841-00). We are grateful to the staff of the TRAO who helped to operate the telescope. The TRAO is a facility operated by the KASI.

Software: Starlink (T. Jenness et al. 2013), GILDAS/CLASS (J. Pety 2005; T. Gildas 2013)

Appendix A Observing Targets

Here we describe information about the targets, such as their star-forming activities, distances, and the measurements of the LOS and POS magnetic field strengths.

A.1. W3OH

W3OH is one of the active star-forming sites in the W3 giant molecular cloud (GMC; A. Rivera-Ingraham et al. 2013), which contains a young ultracompact H II (UC H II) region and rich OH masers (J. W. Dreher & W. J. Welch 1981). There is a water maser source named W3 (H₂O) at $\sim 6''$ east of W3OH, where a hot core with a young massive protobinary system is located (H.-R. Chen et al. 2006). The distance of W3OH is given to be $2.0^{+0.29}_{-0.23}$ kpc from the measurement of Gaia-DR2 parallaxes of OB stars in W3 GMC (F. Navarete et al. 2019).

A CN Zeeman measurement has been made to estimate the LOS magnetic field strength of 1.10 ± 0.33 mG toward W3OH (E. Falgarone et al. 2008). Dust polarization measurements toward W3OH have been made by the 10 m Heinrich Hertz Telescope and JCMT at 1.3 and 0.85 mm, respectively (J. Glenn et al. 1999; B. C. Matthews et al. 2009). However, there is no published result yet on the POS magnetic field strength toward this source.

A.2. OMC-1

OMC-1 is located in Orion A molecular cloud at $388 \text{ pc} \pm 5$, which is the nearest high-mass star-forming region (M. Kounkel et al. 2017). In this region, there are two dense clumps, the Becklin–Neugebauer–Kleinmann–Low (BN/KL) at the northern place and the Orion S at the southern place of the OMC-1 (Figure 3; D. E. Kleinmann & F. J. Low 1967; E. E. Becklin & G. Neugebauer 1967; W. Batria et al. 1983; A. D. Haschick & W. A. Baan 1989). The BN/KL clump is known to contain explosive molecular outflow activities, which are believed to be made by the interaction of young stars in the core of the clump or a protostellar merger (J. Bally & H. Zinnecker 2005; L. Gómez et al. 2005).

Magnetic field strengths in the OMC-1 have been estimated using the Zeeman effect and dust polarization. The LOS magnetic field strengths were measured to be in the range from 0.38 to 16 mG through the Zeeman effect measurements of CN and OH masers (e.g., K. J. Johnston et al. 1989; R. J. Cohen et al. 2006; E. Falgarone et al. 2008). The POS magnetic field strengths have been estimated to be from 0.8 to 26.4 mG through the measurements of dust polarization using interferometry and single dish observations (e.g., M. Houde et al. 2009; K. Pattle et al. 2017; D. T. Chuss et al. 2019; J. A. Guerra et al. 2021; J. Hwang et al. 2021). The LOS and POS magnetic field strengths in our observed region were

measured to be 0.36 and 4.5 mG by the CN Zeeman effect and dust polarization observations using the IRAM and the JCMT, respectively (E. Falgarone et al. 2008; J. Hwang et al. 2021). The LOS magnetic field strength is given as a mean value of the CN Zeeman measurements within a circular IRAM beam size. The beam sizes of the IRAM and the JCMT are $23''$ and $14''$ at 113 and 353 GHz, respectively.

A.3. NGC 2024

NGC 2024 is an active star-forming region in Orion B molecular cloud and associated with a H II region, a massive star cluster, ionizing B stars, and stars at various phases of evolution (P. G. Mezger et al. 1988; E. A. Lada et al. 1991; C. J. Chandler & J. E. Carlstrom 1996). The H II region is located in front of the molecular ridge of NGC 2024 (B. C. Matthews et al. 2002). We adopted the distance of 358.3 ± 15.0 pc for NGC 2024, which was determined by the proper motions of stellar substructures in the Orion Complex with Gaia EDR3 (C. Swiggum et al. 2021).

The POS magnetic field strength is estimated to be 2.2 mG by using the BIMA at the position of a protostellar source FIR 5, which is selected as the central position of our TRAO observations (F. O. Alves et al. 2011). The beam size of the BIMA observations is $2''.45 \times 1''.48$, which is much smaller than that of the CN Zeeman observations. B. C. Matthews et al. (2002) made dust polarization observations toward NGC 2024 using the SCUPOL on the JCMT, from which the POS magnetic field strength was measured to be $56 \mu\text{G}$.

A.4. Mon R2

Mon R2 is a hub-filament system containing a central massive hub and several filaments converged toward the hub (T. S. M. Rayner et al. 2017; S. P. Treviño-Morales et al. 2019; M. S. N. Kumar et al. 2022) and located at the distance of 778 ± 42 pc which is given by the measurement with Gaia DR1 data (C. Zucker et al. 2019). In the central hub, there are five IRS sources, an ultracompact H II region, and gravitationally bounded multiple cores (T. S. M. Rayner et al. 2017). The central hub shows a rotating flattened structure and is connected with filaments where longitudinal gas flow exists toward the hub (S. P. Treviño-Morales et al. 2019).

The measured LOS magnetic field strengths using OH masers are in the range from 0.003 to 0.4 mG (G. R. Knapp & R. L. Brown 1976). There has been no LOS strength measurement using the CN Zeeman effects toward Mon R2. Since the CN line intensity toward Mon R2 is as strong as that of other targets, it is expected that the CN Zeeman effect can likely be detected. J. Hwang et al. (2021) have obtained the POS magnetic field strengths in Mon R2 with the JCMT observations, which vary from 0.02 to 3.64 mG with a mean value of 1.00 ± 0.06 mG.

A.5. DR21

DR21 is a massive star-forming region located in Cygnus X cloud with a distance of $1.4^{+0.12}_{-0.11}$ kpc (N. Schneider et al. 2006; K. L. J. Rygl et al. 2012). DR21 shows a filamentary ridge structure (e.g., N. Schneider et al. 2010) and contains a massive dense core. DR21(OH) associated with various masers (L. A. Zapata et al. 2012) is located at peak intensity positions of CN and dust emission distributions shown in Figure 6.

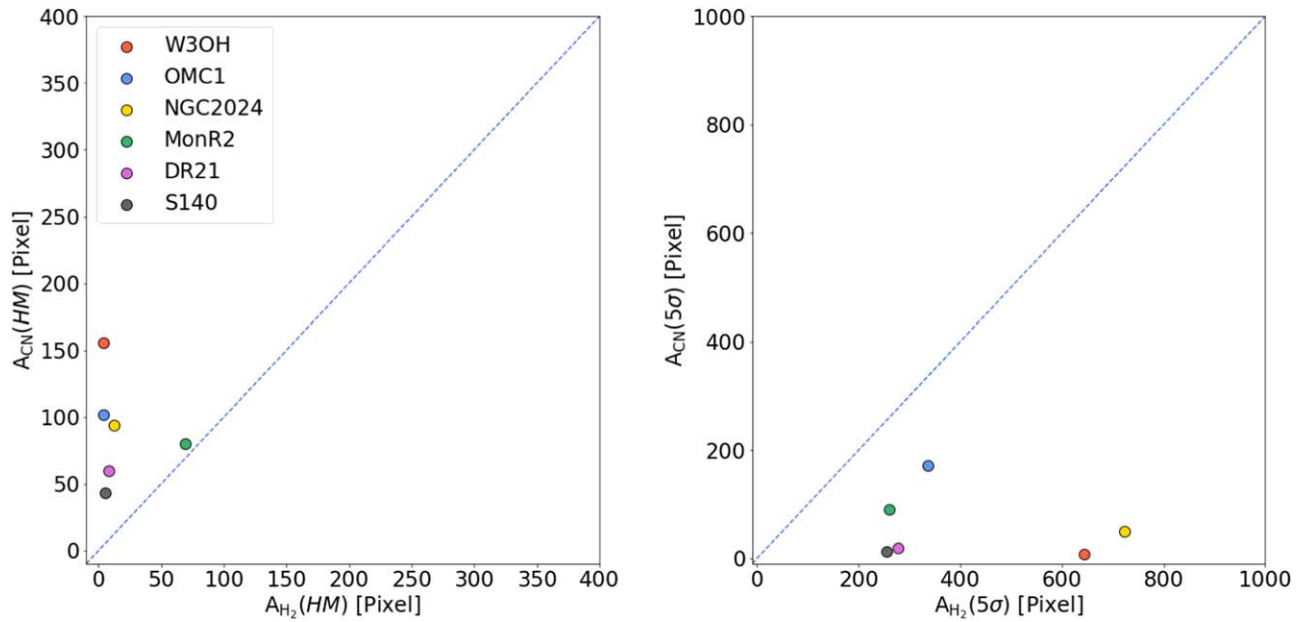


Figure 9. Comparison for the areas within HM contours (left) and $>5\sigma$ level contour level (right) in H_2 and CN column density distributions for the targets. The blue dashed lines represent the lines where the areas obtained from the CN and H_2 column density maps are the same.

The measured LOS magnetic field strength using OH absorption is 0.13 mG (A. Koley et al. 2021). E. Falgarone et al. (2008) have estimated magnetic field strengths of 0.36 and 0.71 mG at two positions of DR21(OH) using the CN Zeeman effects. The POS magnetic field strength is measured to be 0.63 ± 0.18 mG at the north region of DR21 containing DR21(OH) (T.-C. Ching et al. 2022).

A.6. S140

S140 is located at the molecular cloud L1204 at the edge of the Cepheus ring, which is believed to be formed by supernova explosions and stellar winds from the massive stars (M. Kun et al. 1987; T. Preibisch & M. D. Smith 2002). S140 contains a diffuse H II region and photodissociation region created by a B0V star (HD 211880) at the edge of the molecular cloud L1204 (D. Crampton & W. A. Fisher 1974). P. M. Harvey et al. (2012) resolved infrared sources in S140 using the FORCAST camera on the Stratospheric Observatory for Infrared Astronomy (SOFIA). The distance of S140 is suggested to be 906 ± 5 pc with Gaia DR3 data (M. Szilagyi et al. 2023).

OH and CN Zeeman observations measured the LOS magnetic field strengths of 2.8 and 0.25 ± 0.09 mG, respectively (A. Baudry et al. 1997; E. Falgarone et al. 2008). The POS magnetic field strength for this target was measured to be ~ 0.4 mG by the DCF method using JCMT observations (R. L. Curran & A. Chrysostomou 2007).

Appendix B

Comparison of CN- and Dust-emitting Areas

Here we compare the CN- and dust-emitting areas enclosed with two different contour levels for the targets. The one is to use the HM contours for two column densities. The comparison can be made with the areas enclosed with the HM contours for two column density distributions, as shown in the left panel of Figure 9. The HM contour areas of CN column density are at least 7 times larger than the H_2 HM contour areas for all targets, except for Mon R2 for which The HM contour areas of CN

column density are comparable to the H_2 HM contour areas. The other one is to use the 5σ contour level for the comparison of low-density parts in the targets. As shown in the right panel of Figure 9, all targets have the area within the H_2 column density contour of $>5\sigma$ level much larger than the area of the CN column density contour with $>5\sigma$ level.

ORCID iDs

Jihye Hwang <https://orcid.org/0000-0001-7866-2686>
 Chang Won Lee <https://orcid.org/0000-0002-3179-6334>
 Jongsoo Kim <https://orcid.org/0000-0002-1229-0426>
 Eun Jung Chung <https://orcid.org/0000-0003-0014-1527>
 Kee-Tae Kim <https://orcid.org/0000-0003-2412-7092>

References

- Alves, F. O., Girart, J. M., Lai, S.-P., et al. 2011, *ApJ*, 726, 63
 Andersson, B.-G., Lazarian, A., & Vaillancourt, J. E. 2015, *ARA&A*, 53, 501
 André, P., Men'shchikov, A., Bontemps, S., et al. 2010, *A&A*, 518, L102
 Bally, J., & Zinnecker, H. 2005, *AJ*, 129, 2281
 Batria, W., Wilson, T. L., Bastien, P., et al. 1983, *A&A*, 128, 279
 Baudry, A., Desmurs, J. F., Wilson, T. L., et al. 1997, *A&A*, 325, 255
 Becklin, E. E., & Neugebauer, G. 1967, *ApJ*, 147, 799
 Beckwith, S. V. W., Sargent, A. I., Chini, R. S., et al. 1990, *AJ*, 99, 924
 Chandler, C. J., & Carlstrom, J. E. 1996, *ApJ*, 466, 338
 Chandrasekhar, S., & Fermi, E. 1953, *ApJ*, 118, 113
 Chen, H.-R., Welch, W. J., Wilner, D. J., et al. 2006, in ASP Conf. Ser. 356, Revealing the Molecular Universe: One Antenna is Never Enough, ed. D. C. Backer, J. W. Moran, & J. L. Turner (San Francisco, CA: ASP), 270
 Ching, T.-C., Qiu, K., Li, D., et al. 2022, *ApJ*, 941, 122
 Chuss, D. T., Andersson, B.-G., Bally, J., et al. 2019, *ApJ*, 872, 187
 Cohen, R. J., Gasprong, N., Meaburn, J., & Graham, M. F. 2006, *MNRAS*, 367, 541
 Coudé, S., Bastien, P., Houde, M., et al. 2019, *ApJ*, 877, 88
 Crampton, D., & Fisher, W. A. 1974, *PDAO*, 14, 283
 Crutcher, R. M., & Kemball, A. J. 2019, *FrASS*, 6, 66
 Crutcher, R. M., Nutter, D. J., Ward-Thompson, D., et al. 2004, *ApJ*, 600, 279
 Curran, R. L., & Chrysostomou, A. 2007, *MNRAS*, 382, 699
 Davis, L. 1951, *PhRv*, 81, 890
 Doi, Y., Hasegawa, T., Furuya, R. S., et al. 2020, *ApJ*, 899, 28
 Doi, Y., Tomisaka, K., Hasegawa, T., et al. 2021, *ApJL*, 923, L9
 Dreher, J. W., & Welch, W. J. 1981, *ApJ*, 245, 857

- Falgarone, E., Troland, T. H., Crutcher, R. M., & Paubert, G. 2008, *A&A*, **487**, 247
- Fixsen, D. J. 2009, *ApJ*, **707**, 916
- Friberg, P., Bastien, P., Berry, D., et al. 2016, *Proc. SPIE*, **9914**, 991403
- Gildas, T., 2013 GILDAS: Grenoble Image and Line Data Analysis Software, Astrophysics Source Code Library,, ascl:[1305.010](#)
- Glenn, J., Walker, C. K., & Young, E. T. 1999, *ApJ*, **511**, 812
- Gómez, L., Rodríguez, L. F., Loinard, L., et al. 2005, *ApJ*, **635**, 1166
- Goodman, A. A., Crutcher, R. M., Heiles, C., et al. 1989, *ApJL*, **338**, L61
- Goodman, A. A., & Heiles, C. 1994, *ApJ*, **424**, 208
- Griffin, M. J., Abergel, A., Abreu, A., et al. 2010, *A&A*, **518**, L3
- Guerra, J. A., Chuss, D. T., Dowell, C. D., et al. 2021, *ApJ*, **908**, 98
- Harvey, P. M., Adams, J. D., Herter, T. L., et al. 2012, *ApJL*, **749**, L20
- Haschick, A. D., & Baan, W. A. 1989, *ApJ*, **339**, 949
- Hildebrand, R. H. 1983, *QJRAS*, **24**, 267
- Hily-Blant, P., Walmsley, M., Pineau Des Forêts, G., & Flower, D. 2008, *A&A*, **480**, L5
- Holland, W. S., Bintley, D., Chapin, E. L., et al. 2013, *MNRAS*, **430**, 2513
- Houde, M., Vaillancourt, J. E., Hildebrand, R. H., Chitsazzadeh, S., & Kirby, L. 2009, *ApJ*, **706**, 1504
- Hwang, J., Kim, J., Pattle, K., et al. 2021, *ApJ*, **913**, 85
- Hwang, J., Kim, J., Pattle, K., et al. 2022, *ApJ*, **941**, 51
- Jenness, T., Chapin, E. L., Berry, D. S., et al., 2013 SMURF: SubMillimeter User Reduction Facility, Astrophysics Source Code Library,, ascl:[1310.007](#)
- Jeong, I.-G., Kang, H., Jung, J., et al. 2019, *JKAS*, **52**, 227
- Johnston, K. J., Migenes, V., & Norris, R. P. 1989, *ApJ*, **341**, 847
- Kirk, J. M., Ward-Thompson, D., Palmeirim, P., et al. 2013, *MNRAS*, **432**, 1424
- Kleinmann, D. E., & Low, F. J. 1967, *ApJL*, **149**, L1
- Knapp, G. R., & Brown, R. L. 1976, *ApJ*, **204**, 21
- Koley, A., Roy, N., Menten, K. M., et al. 2021, *MNRAS*, **501**, 4825
- Kounkel, M., Hartmann, L., Loinard, L., et al. 2017, *ApJ*, **834**, 142
- Kumar, M. S. N., Arzoumanian, D., Men'shchikov, A., et al. 2022, *A&A*, **658**, A114
- Kun, M., Balazs, L. G., & Toth, I. 1987, *Ap&SS*, **134**, 211
- Lada, E. A., Depoy, D. L., Evans, N. J., et al. 1991, *ApJ*, **371**, 171
- Lazarian, A., & Hoang, T. 2007, *MNRAS*, **378**, 910
- Mangum, J. G., & Shirley, Y. L. 2015, *PASP*, **127**, 266
- Mathews, B. C., Fiege, J. D., & Moriarty-Schieven, G. 2002, *ApJ*, **569**, 304
- Mathews, B. C., McPhee, C. A., Fissel, L. M., et al. 2009, *ApJS*, **182**, 143
- Mathews, B. C., & Wilson, C. D. 2002, *ApJ*, **574**, 822
- Mezger, P. G., Chini, R., Kreysa, E., et al. 1988, *A&A*, **191**, 44
- Motte, F., & André, P. 2001, *A&A*, **365**, 440
- Mouschovias, T. C., & Spitzer, L. 1976, *ApJ*, **210**, 326
- Mouschovias, T. C., Tassis, K., & Kunz, M. W. 2006, *ApJ*, **646**, 1043
- Myers, P. C., & Goodman, A. A. 1991, *ApJ*, **373**, 509
- Nakano, T., & Nakamura, T. 1978, *PASJ*, **30**, 671
- Navarete, F., Galli, P. A. B., & Damineli, A. 2019, *MNRAS*, **487**, 2771
- Pattle, K., & Fissel, L. 2019, *FrASS*, **6**, 15
- Pattle, K., Fissel, L., Tahani, M., et al. 2023, in ASP Conf. Ser. 534, Protostars and Planets VII (San Francisco, CA: ASP), 193
- Pattle, K., Ward-Thompson, D., Berry, D., et al. 2017, *ApJ*, **846**, 122
- Pety, J. 2005, in SF2A-2005: Semaine de l'Astrophysique Francaise, ed. F. Casoli et al. (Les Ulis: EDP Sciences), 721
- Pickett, H. M., Poynter, R. L., Cohen, E. A., et al. 1998, *JQSRT*, **60**, 883
- Pillai, T., Kauffmann, J., Wiesemeyer, H., & Menten, K. M. 2016, *A&A*, **591**, A19
- Poglitsch, A., Waelkens, C., Geis, N., et al. 2010, *A&A*, **518**, L2
- Preibisch, T., & Smith, M. D. 2002, *A&A*, **383**, 540
- Rayner, T. S. M., Griffin, M. J., Schneider, N., et al. 2017, *A&A*, **607**, A22
- Rivera-Ingraham, A., Martin, P. G., Polychroni, D., et al. 2013, *ApJ*, **766**, 85
- Rygl, K. L. J., Brunthaler, A., Sanna, A., et al. 2012, *A&A*, **539**, A79
- Schneider, N., Bontemps, S., Simon, R., et al. 2006, *A&A*, **458**, 855
- Schneider, N., Csengeri, T., Bontemps, S., et al. 2010, *A&A*, **520**, A49
- Swiggum, C., D'Onghia, E., Alves, J., et al. 2021, *ApJ*, **917**, 21
- Szilagyi, M., Kun, M., Abraham, P., & Marton, G. 2023, *MNRAS*, **520**, 1390
- Treviño-Morales, S. P., Fuente, A., Sánchez-Monge, A., et al. 2019, *A&A*, **629**, A81
- Turner, B. E., & Gammon, R. H. 1975, *ApJ*, **198**, 71
- Zapata, L. A., Loinard, L., Su, Y.-N., et al. 2012, *ApJ*, **744**, 86
- Zucker, C., Speagle, J. S., Schlafly, E. F., et al. 2019, *ApJ*, **879**, 125